

T-wave Inversion through Inhomogeneous Voltage Diffusion within the FK3V Cardiac Model

E. Angelaki^{1,2}, N. Lazarides³, G. D. Barmparis¹, Ioannis Kourakis³, Maria E. Marketou^{4,5}, G. P. Tsironis^{1,2}

¹*Department of Physics, and Institute of Theoretical and Computational Physics, University of Crete, Heraklion, Greece*

²*Harvard John A. Paulson School of Engineering and Applied Sciences, Harvard University, Cambridge, MA, USA*

³*Department of Mathematics, Khalifa University of Science and Technology, P.O. Box 127788, Abu Dhabi, United Arab Emirates*

⁴*School of Medicine, University of Crete, Heraklion, Greece and*

⁵*Department of Cardiology, Heraklion University Hospital, Heraklion, Greece*

(Dated: November 15, 2023)

The heart beats due to the synchronized contraction of cardiomyocytes triggered by a periodic sequence of electrical signals called action potentials, which originate in the sinoatrial node and spread through the heart's electrical system. A large body of work is devoted to modeling the propagation of the action potential and to reproducing reliably its shape and duration. Connection of computational modeling of cells to macroscopic phenomenological curves such as the electrocardiogram has been also intense, due to its clinical importance in analysing cardiovascular diseases. In this work we simulate the dynamics of action potential propagation using the three-variable Fenton-Karma model that can account for both normal and damaged cells through spatially inhomogeneous voltage diffusion coefficient. We monitor the action potential propagation in the cardiac tissue and calculate the pseudo-electrocardiogram that reproduces the R and T waves. The R wave amplitude varies according to a double exponential law as a function of the (spatially homogeneous, for an isotropic tissue) diffusion coefficient. The addition of spatial inhomogeneity in the diffusion coefficient by means of a defected region representing damaged cardiac cells, may result in T-wave inversion in the calculated pseudo-electrocardiogram. The transition from positive to negative polarity of the T-wave is analyzed as a function of the length and the depth of the defected region.

Cardiovascular diseases (CVDs) are the leading cause of death globally. The healthy heart produces a synchronized mechanical contraction by a self-generated electrical signal that propagates through the muscle as an action potential (AP) wave, and is tracked through the electrocardiogram (ECG), perhaps the most widely used clinical tool for the detection and diagnosis of a broad range of cardiac conditions. The last decades, there has been a fast growth of sophisticated and detailed mathematical models that encompass realistic electrophysiological and anatomical properties, aiming to help understanding life-threatening situations related to CVDs and developing appropriate therapies. Moreover, significant progress has been achieved in solving the forward problem of electrocardiography to obtain the simulated ECG (i.e., the pseudo-ECG) of a patient. The detailed computational models, however, often defy simple mathematical analysis and transparency; fortunately, the more flexible lower-dimensional phenomenological (“simple”) models, such as the three-variable Fenton-Karma (FK3V) model, can reproduce quantitatively the overall characteristics of cardiac tissue that are relevant to the AP propagation. Importantly, a pseudo-ECG can be calculated from the action potentials obtained from the FK3V model, which reproduce some features of observed ECGs. Specifically, they reproduce the R and T wave, as well as the T-wave inversion commonly found in myocardial ischemia. In that condition, the electric conductance in a particular region of the cardiac tissue (scar) is severely reduced. Within the FK3V model, this situation can be described by inhomogeneous voltage diffusion coefficient with very low value in the region of the scar. For sufficiently large scar, the polarization of the T wave is inverted from positive to negative, providing thus a strong link between a phenomenological quantity and measured data. That link of the inverted T-

wave and the inhomogeneous diffusion coefficient (i.e., the diffusion coefficient with a defected region representing a scar) may be used in identifying the location and the width of the scar by solving the inverse problem, which may be a matter of future research.

I. INTRODUCTION

The heart is a muscular organ situated between the right and left lungs whose primary role is to pump oxygen-rich blood throughout the body. It has four main chambers; the two smaller upper ones are called atria, and the larger lower ones are called ventricles. Life is sustained due to the reliable propagation of action potentials (AP) across the cardiac muscle, or myocardium, which ensures its coordinated excitation and contraction, i.e., the heartbeat. The AP is essentially an electrical disturbance, which propagates over long distances preserving its amplitude. Once initiated by excitation from a stimulus current, its propagation becomes independent of the triggering stimulus, achieving thus an “autopreserving” status. To initiate the AP, the triggering stimulus current must assume a threshold value of certain amplitude and duration.

Cardiac cells, called myocytes, are roughly shaped as cylinders $100\mu\text{m}$ long and $25\mu\text{m}$ wide [1], and are metabolically and electrically connected via gap junctions [2]. Action potential propagation involves the diffusion of ions between cells via these gap junctions, as well as their transfer in and out of the cell via transmembrane ionic currents. Effectively, gap junctions slow down propagation by having a larger resistance than the cytoplasm. Gap junctions allow heart cells to function in a coordinated, synchronized manner, ensuring they are electrically connected as a single unit. These junctions are predominantly found at the ends of cells. As a result, the

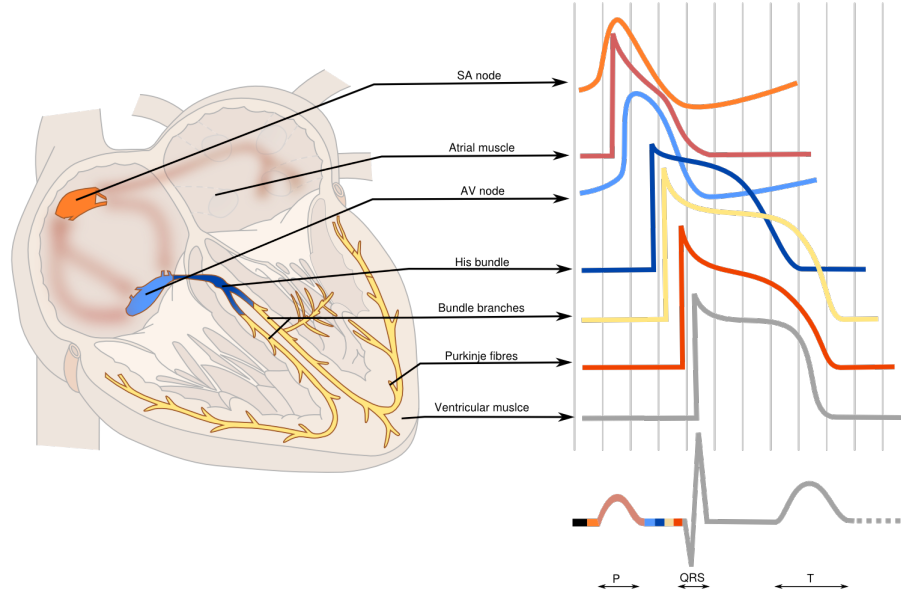


FIG. 1: Cardiac action potential shown for different types of cardiomyocytes, whose names are shown on the arrows, and how they relate to the electrocardiogram. Image courtesy of Dr. De Voogt and ECGpedia.org

anatomic characteristics of groups of cardiac muscle differ based on the orientation they are studied from, a trait known as “anisotropy”. Conduction velocity is typically faster, about two to three times, along the length of the fiber compared to across its width.

Cardiac electrical propagation is often modeled as a reaction-diffusion process. Ionic models that describe this process have become increasingly more complex and more realistic. For the ventricular AP across mammalian cardiac cells, several ionic models with simplified ionic currents have been developed, reviewed in a recent article [3]. The mathematical aspects of cardiac electrophysiology have been exposed in Ref. [4], while the computing aspects in Refs. [5, 6]. Two such models are the three-variable cardiac Fenton-Karma (FK3V) model [7], and the four-variable Bueno-Cherry-Fenton model [8], which have been shown previously to be highly useful for reproducing a broad range of dynamics of cardiac cells and tissue obtained experimentally or from other more complex models. Recently, the FK3V model was used in the reconstruction of cardiac electrical excitations from optical mapping recordings [9], while a three-dimensional anisotropic version of it was used to simulate vortices in the lower heart chambers [10]. Moreover, an extension of the FK3V model that accounts for stochastic effects has been reported [11]. We should also mention the more involved electrophysiological models such as the Beeler-Reuter model [12], the Luo-Rudy model [13], and the TenTusscher-Noble-Noble-Panfilov model [14], which are based on direct experimental observations. These models, though, are too complex

to provide an essential phenomenological insight into the spatial dynamical behavior of the AP, and this is the reason we chose the FK3V model.

A macroscopic depiction of the cardiac electrical activity is the electrocardiogram (ECG) tracing, a relatively inexpensive and widely available medical screening tool. Recorded using a machine called an electrocardiograph, it is the primary evaluation method for a person suspected of having a cardiovascular pathology [15, 16]. Analysis of the ECG using various methods has helped clinicians detect cardiovascular abnormalities [17], e.g., one study uses a single (out of the usually acquired 12) lead in an ECG, to detect T-wave (ventricular repolarisation) morphology abnormalities [18].

Fig. 1 shows the cardiac conduction system as a network of specialized cells comprising of the sinoatrial node, the atrial muscle, the atrioventricular node, the His bundle and its bundle branches, the Purkinje fibers, and finally the ventricular myocytes. Depicted is the membrane potential with respect to time, for the duration of a single heartbeat. Note that AP curve shapes are different for each type of cardiac cell. P waves relate to the depolarization of the atrial myocytes, the QRS complex relates to the depolarization of the ventricles, and T waves relate to the repolarization of the ventricles. We notice that, the AP of the ventricular cells, depicted by the grey curve at the bottom of the series of curves, has a longer duration than that of the sinoatrial node, drawn as the top curve; also, the Purkinje cell AP is similar to the ventricular action potential except for a sharper initial peak. These relations are color-coded in the small realistic ECG at the bottom right of

the image. Disruptions in AP propagation are the manifestations of underlying cardiac abnormalities; in myocardial ischemia, for example, the blood supply to the heart's coronary arteries cannot meet the demand.

The basis of ischemic arrhythmogenesis is the alteration in the electrical properties of ventricular tissue, producing changes in the AP pulse morphology and the body surface ECG [19, 20]. One such alteration, the remodeling of ionic currents due to changes in intracellular and extracellular ionic concentrations, has been studied in the literature [21]. In addition to ionic remodeling, spatial heterogeneity such as cell-to-cell decoupling, occurring usually in later stages of ischemia, has been shown experimentally to lead to propagation disruptions and a reduction in conduction velocity [22].

In this work, we perform extensive simulations using the FK3V model for the ventricular AP over a one-dimensional (1D) cable transversal to the ventricular tissue. The obtained AP is then used to generate a related ECG pattern, usually called a pseudo-ECG [23, 24], whose morphology under different values and profiles of the voltage diffusion coefficient is then explored. We mimic a spatially localized area of depressed conductivity by reducing the diffusion coefficient considerably in that specific area. Within the framework of the FK3V model we were able to reproduce the R and T waves of the ECG through appropriately adjusting the characteristics of the stimulus current. Moreover, the calculated pseudo-ECG exhibits T-wave inversion which may become deep for relatively large scar tissue areas in the heart, in a way resembling what has been observed for patients with myocardial ischemia. For simplicity, only one set of electrophysiological parameters is used, i.e., the cable spans a single region of the ventricular tissue.

One-dimensional numerical simulations, being quick and efficient, enabled us to try out multiple different values for the relevant parameters and capture the changes in morphology. The aforementioned property of conduction velocity being typically about two to three times faster along the length of the fiber compared to across its width, makes numerical calculations using 1D models a good first approach.

II. METHODS

A. The three variable model by Fenton and Karma

Computational models allow the study of AP propagation in single cells, in 1D cables of cells, in two-dimensional slabs of tissue, as well as in three-dimensional whole heart models. The FK3V model of coupled reaction-diffusion equations on a 1D cable of cells is used in this work to produce pseudo-ECG patterns relating to AP propagation. We present the equations briefly here; for a detailed presentation one may consult the original article by Fenton and Karma [7] or the review article by Alonso *et al.* [3].

Our theoretical cable of cells, of length $L = 3$ cm, is composed of 400 ventricular cells of a single cell type, connected via gap junctions. A stimulus current $J_{\text{stim}}(x, t)$ with an above-threshold amplitude is applied to the first 15 cells (i.e., with

the first cell being at $x = 0$). That current is therefore assumed to excite a small, spatially restricted region around the left end of the cable of length $L_{\text{exc}} = 15 \times \langle \text{cell length} \rangle$. We take the cardiac cell length to be equal to the spatial discretization $dx = 0.0075$ cm, so that $L_{\text{exc}} \simeq 0.11$ cm. In what follows, the stimulus current J_{stim} is taken to be a rectangular pulse of amplitude $J_{\text{amp}} = 0.9$ mA and duration $\tau_p = 11$ ms, unless otherwise stated. The model consists of the three coupled partial differential equations (for completeness the stimulus current is also included)

$$\frac{\partial u}{\partial t} = \nabla \cdot (\tilde{D} \nabla u) - J_{\text{fi}}(u; v) - J_{\text{so}}(u) - J_{\text{si}}(u; w) + J_{\text{stim}}(x, t) \quad (1)$$

$$\frac{\partial v}{\partial t} = \Theta(u_c - u) \frac{1 - v}{\tau_v^-(u)} - \Theta(u - u_c) \frac{v}{\tau_v^+} \quad (2)$$

$$\frac{\partial w}{\partial t} = \Theta(u_c - u) \frac{1 - w}{\tau_w^-} - \Theta(u - u_c) \frac{w}{\tau_w^+} \quad (3)$$

The normalized transmembrane voltage function $u(x, t)$ is obtained through the relation

$$u(x, t) \equiv \frac{V(x, t) - V_0}{V_{fi} - V_0}, \quad (4)$$

where $V(x, t)$ is the un-normalized transmembrane potential measured in units of mV, V_0 is the resting membrane potential, and V_{fi} is the Nernst potential of the fast inward current. The normalized threshold potential is given by u_c .

The permeability of the channels in the cell membrane is regulated by the two gating variables $v(x, t)$ and $w(x, t)$. Gate state indicates whether ions can pass through the membrane or not. The variable $v(x, t)$ denotes the fast inactivation gate which opens when the cell is not excited, and closes when it becomes excited. The closing time constant τ_v^+ corresponds to cell depolarization, and the opening time constant τ_v^- to cell repolarization. The u -dependent parameter $\tau_v^-(u)$ is given by

$$\tau_v^-(u) = \Theta(u - u_v) \tau_{v1}^- + \Theta(u_v - u) \tau_{v2}^-. \quad (5)$$

This splitting allows the minimum diastolic interval, i.e., the excitable gap, controlled by τ_{v1}^- , to vary independently from the steepness of this curve, controlled by τ_{v2}^- . The voltage threshold $u_c > u_v$ controls the splitting. The variable w is the probability of a gate opening as described in the Hodgkin-Huxley model [25]; τ_w^+ and τ_w^- are the time constants for closing and opening of the gate, respectively.

The scaled phenomenological ionic currents J_{fi} , J_{so} , and J_{si} , where the subscript f means fast and s slow, are related to the corresponding currents in units of mA through

$$J_i = \frac{I_i}{C_m (V_i - V_0)} \quad (6)$$

where C_m is the membrane capacitance, and i represents any of the different fi, so, or si. The following remarks on the currents are worth to be made:

Parameter	BR model	MBR model	MLR-I model
\bar{g}_{fi}	4	4	5.8
τ_r	33.33	50	130
τ_{si}	29	44.84	127
τ_0	12.5	8.3	12.5
τ_v^+	3.33	3.33	10
τ_{v1}^-	1250	1000	18.2
τ_{v2}^+	19.6	19.2	18.2
τ_w^+	870	667	1020
τ_w^-	41	11	80
u_c	0.13	0.13	0.13
u_v	0.04	0.055	—
u_c^{si}	0.85	0.85	0.85
Other Parameters			
C_m	$1 \mu\text{F}/\text{cm}^2$		
V_0	-85 mV		
V_{fi}	$+15 \text{ mV}$		
k	10		

TABLE I: Three different sets of model parameters that can be used into the three-variable Fenton-Karma model (Eqs. (1) - (3)). In this work, the parameters of the modified Beeler-Reuter (MBR) model parameters are used (from Ref. [26]).

(a) J_{fi} corresponds to the fast inward sodium (Na^+) current, responsible for the depolarization of the membrane, and depending on the gating variable v . This gating variable is responsible for inactivation of the current after depolarization, and its reactivation after repolarization,

(b) J_{so} is a slow outward current analogous to the time-independent potassium (K^+) current; it is responsible for repolarization of the cell membrane, and

(c) J_{si} is a slow inward current, corresponding to the calcium (Ca^+) current, that balances I_{so} during the plateau phase of the AP; this current depends on one gate variable w , responsible for its inactivation and reactivation.

The above correspondence to the Na, K, and Ca currents is certainly an oversimplification, due to membrane dynamics being a lot more complex. The model, though, succeeds in capturing the minimal ionic complexity that underlies the membrane recovery processes. All currents are considered normalized. The expressions for the normalized currents read

$$J_{fi}(u; v) = -\frac{v}{\tau_d} \Theta(u - u_c)(1 - u)(u - u_c), \quad (7)$$

$$J_{so}(u) = +\frac{u}{\tau_0} \Theta(u_c - u) + \frac{1}{\tau_{extr}} \Theta(u - u_c) \quad (8)$$

$$J_{si}(u; w) = -\frac{w}{2\tau_{si}} \left\{ 1 + \tanh \left[k(u - u_c^{si}) \right] \right\}, \quad (9)$$

where

$$\tau_d = \frac{C_m}{\bar{g}_{fi}}. \quad (10)$$

The values of the parameters \bar{g}_{fi} , τ_0 , τ_r , τ_{si} , k , and u_c^{si} are given in Table I. In this work, the values of the modified Beeler-Reuter (MBR) model parameters are used in the FK3V equations. The function $\Theta = \Theta(x)$, which appears repeatedly in Eqs. (1)-(3) and Eqs. (7)-(9), is the standard Heaviside step

function defined by $\Theta(x) = 1$ for $x \geq 0$ and $\Theta(x) = 0$ for $x < 0$. Note that the parenthesis next to the symbol Θ , i.e., $\Theta(u - u_c)$, is not a multiplicand but the argument of the function.

From Eq. (1) we can see that modeling the propagation of electrical impulses in cardiac tissue is affected by two distinct terms. The first term of the right hand side, includes the diffusion coefficient and encompasses the passive characteristics of the medium, such as its microscopic structure and cell-to-cell coupling via ion conducting gap junctions [27]. The second term, the sum of the ionic currents through the membrane channels (excluding the stimulus current J_{stim}), denotes the dynamic characteristic of the medium. As mentioned above, most of the research on propagation disruptions concentrates on the remodeling of ionic currents. We chose to concentrate on varying the profiles of the voltage diffusion coefficient and consequently studying their effect on the calculated pseudo-ECG, regarding thus the suppression of electrical connection between cells as the primary cause of cardiac pathology. More detailed ionic models may include more membrane currents measured in classic voltage-clamp or patch-clamp experiments, and a larger number of gates.

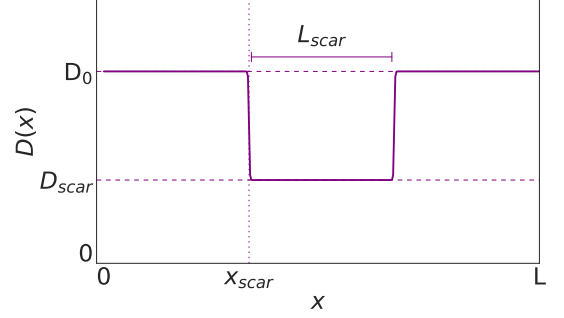


FIG. 2: Profile of the diffusion coefficient $D(x) > 0$ ($0 < x < L$) for a localized defect of width L_{scar} and decrease percentage λ , around the effective D_0 in the regions where the tissue is normal (healthy). The dotted vertical line highlights the start x_{scar} of the defected region (scar). The parameter values used to make this particular plot are $D_0 = 0.005 \text{ cm}^2 \text{ms}^{-1}$, $L_{scar} = 1.0 \text{ cm}$, $x_{scar} = 1.0 \text{ cm}$, $\lambda = -0.6$, and $L = 3.0 \text{ cm}$. Using Eq. (12) we find $D_{scar} = 0.002 \text{ mV}$.

B. The Role of the Diffusion Coefficient

From the cable equation analysis, the effective voltage diffusion coefficient for homogeneous (healthy) tissue is given by

$$D_0 = \frac{1}{C_m \rho S_u} \quad (11)$$

where C_m is the cell membrane capacitance, ρ is the longitudinal resistivity (attributed to the gap junctions), and S_u is the surface-to-volume ratio for the cell. The values of the parameters $C_m = 1 \mu\text{F}/\text{cm}^2$, $\rho = 0.4 \text{ k}\Omega\text{cm}$ (experimentally measured [8]), and $S_u = 5000 \text{ cm}^{-1}$ provided in Table I for human ventricular cells, give the typical value $D_0 =$

$0.0012 \pm 0.0002 \text{ cm}^2\text{ms}^{-1}$ used often in literature. In this work we use various values for the diffusion coefficient, and by doing so, we can model various sub-cellular characteristics of cardiac electrical propagation, such as different gap junction resistance and cell membrane capacitance, and by extension, study conduction problems in the heart. Myocardial tissue is, of course, a very complex structure, and we hope to capture only a part of its behavior.

We study the role of the diffusion coefficient both when it is constant, and when it is allowed to vary spatially. In Fig. 2, we plot the profile of the diffusion coefficient $\tilde{D}(x)$ that contains a localized heterogeneity in the form of a defected (scar) region in which the conductance velocity has been significantly reduced due to reduced electrical connection between cells, i.e., a region in which the value of $\tilde{D}(x)$ has dropped to

$$D_{\text{scar}} = (1 + \lambda) D_0, \quad (12)$$

where D_0 is the value of $\tilde{D}(x)$ in the normal (healthy) region, and $-1 < \lambda < 0$. For example, for a cable length of $L = 3.0 \text{ cm}$ with $D_0 = 0.005 \text{ cm}^2\text{ms}^{-1}$, a defected region of length $L_{\text{scar}} = 0.5 \text{ cm}$ and $\lambda = -0.8$ would have $D_{\text{scar}} = 0.001 \text{ cm}^2\text{ms}^{-1}$. Hence, the spatially dependent voltage diffusion coefficient has the form

$$\tilde{D}(x) = \begin{cases} D_{\text{scar}}, & \text{if } x_{\text{scar}} < x < x_{\text{scar}} + L_{\text{scar}} \\ D_0, & \text{anywhere else.} \end{cases} \quad (13)$$

Note that in a recent work [28], a spatially and temporally diffusion coefficient was considered which encompasses conductance heterogeneities in the cardiac tissue induced by the dynamics of the gap junctions. Obviously, the adjustable parameters of the voltage diffusion profile is the starting point of the defected region x_{scar} , the spatial length of the scar tissue L_{scar} , and the percentage decrease $-\lambda$ which lowers $\tilde{D}(x)$ in the defected region. Using Eqs. (12) and (13) above, the spatially averaged diffusion coefficient is

$$\langle \tilde{D}(x) \rangle = D_0 \left(1 + \lambda \frac{L_{\text{scar}}}{L} \right). \quad (14)$$

C. Numerical Calculations

All numerical simulations for Eqs. (1) - (3) along with Eqs. (7) - (9) were performed on a theoretical 1D cable of cells, using the fourth order Runge-Kutta algorithm with fixed time-step $dt = 0.002 \text{ ms}$. For spatially discretizing Eqs. (1) - (3), the spatial domain was divided into $N_x - 1$ elements with $N_x = 400$ nodes at $x_i = (i - 1)L/(N_x - 1)$ ($i = 1, 2, \dots, N_x$) which are separated by distance $dx = L/(N_x - 1) = 0.0075 \text{ cm}$ (about the length of a cardiac cell). Second order, centered finite difference formulas were used to discretize the first and second derivatives of the state variables wherever they appear in Eqs. (1) - (3). The spatially discretized equations are given explicitly in the next subsection. For numerical purposes, the spatially dependent (inhomogeneous) diffusion coefficient $\tilde{D}(x)$ is modeled as a double step-function controlled by two very steep tanh functions. Independent runs were executed using different numerical codes written in Python and

Fortran 95, and the results were verified to be practically the same. Unless otherwise specified, the number of time-steps were 150,000.

The boundary conditions at the ends of the cable are chosen to be those of zero-flux (Neumann) type, i.e.,

$$\tilde{D}(x) \frac{\partial u(x,t)}{\partial x} \Big|_{x=0} = \tilde{D}(x) \frac{\partial u(x,t)}{\partial x} \Big|_{x=L} = 0, \quad (15)$$

where L is the length of the cable which, in what follows, is set everywhere equal to 3 cm ($L = 3.0 \text{ cm}$). As explained above, the (inhomogeneous) diffusion coefficient $\tilde{D}(x)$ is practically a piece-wise constant function which assumes the value D_0 and D_{scar} in the normal (healthy) and defected (scar) tissue region, respectively, as it is shown schematically in Fig. 2.

For a homogeneous (spatially constant) diffusion coefficient $\tilde{D}(x) = \tilde{D}$ along the cable, Eq. (1) becomes

$$\frac{\partial u}{\partial t} = \tilde{D} \cdot \frac{\partial^2 u}{\partial x^2} - J_{\text{fi}} - J_{\text{so}} - I_{\text{si}} + J_{\text{stim}}. \quad (16)$$

If the diffusion coefficient \tilde{D} is allowed to depend on the spatial coordinate x , the first term on the right hand side of Eq. (1), i.e., $\nabla(\tilde{D}\nabla u)$ becomes

$$\frac{\partial}{\partial x} \left[\tilde{D}(x) \frac{\partial u(x,t)}{\partial x} \right] = \frac{\partial \tilde{D}(x)}{\partial x} \frac{\partial u(x,t)}{\partial x} + \tilde{D}(x) \frac{\partial^2 u(x,t)}{\partial x^2}. \quad (17)$$

From Eq. (17) we can see that we need the discrete form of the first and second spatial derivative of $u(x,t)$, as well as the first spatial derivative of $\tilde{D}(x)$. We use the following centered differences [29]

$$\frac{\partial u(x,t)}{\partial x} = \frac{u_{i+1}(t) - u_{i-1}(t)}{2\Delta x}, \quad (18)$$

$$\frac{\partial \tilde{D}(x)}{\partial x} = \frac{\tilde{D}_{i+1} - \tilde{D}_{i-1}}{2\Delta x}, \quad (19)$$

$$\frac{\partial^2 u(x,t)}{\partial x^2} = \frac{u_{i+1}(t) - 2u_i(t) + u_{i-1}(t)}{\Delta x^2}. \quad (20)$$

Using Eqs. (17-18), the spatially discretized system of Eqs. (1-3) reads

$$\begin{aligned} \frac{\partial u_i}{\partial t} = & \frac{\tilde{D}_{i+1} - \tilde{D}_{i-1}}{2\Delta x} \frac{u_{i+1} - u_{i-1}}{2\Delta x} + \tilde{D}(x_i) \frac{u_{i+1} - 2u_i + u_{i-1}}{\Delta x^2} \\ & - J_{\text{fi}}(u_i; v_i) - J_{\text{so}}(u_i) - J_{\text{si}}(u_i; w_i) + J_{\text{stim}}(x_i, t), \end{aligned} \quad (21)$$

$$\frac{\partial v_i}{\partial t} = \Theta(u_c - u_i) \frac{1 - v_i}{\tau_v^-(u_i)} - \Theta(u_i - u_c) \frac{v_i}{\tau_v^+}, \quad (22)$$

$$\frac{\partial w_i}{\partial t} = \Theta(u_c - u_i) \frac{1 - w_i}{\tau_w^-} - \Theta(u_i - u_c) \frac{w_i}{\tau_w^+}, \quad (23)$$

where it is implied that the discretized variables u_i , v_i , and w_i depend on time t . The stimulus current, which is necessary for the excitation of the AP pulse, is assumed to arise from physiological mechanisms of the heart. There is a large volume of works on the calculation of the ventricular AP in 1D [30–33] using various types of stimulus current functions $J_{\text{stim}}(x, t)$. The FK3V model has been also used for the calculation of the ventricular AP in two and three dimensions [34]. Also, mapping models have been used for the analysis of numerical results obtained through the FK3V model [35].

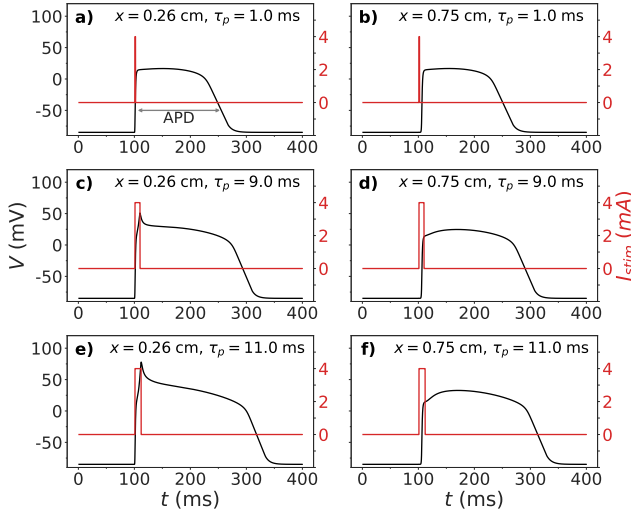


FIG. 3: The action potential V (black curves) in natural units as a function of time t that is produced by a single rectangular current pulse depicted by the red curve (notice the small deflection in the beginning) for $D = 0.005 \text{ cm}^2\text{ms}^{-1}$, $L_{\text{exc}} = 0.113 \text{ cm}$, $J_{\text{amp}} = 4.0 \text{ mA}$. The action potential duration (APD), indicated by the gray horizontal double-headed arrow, is measured for each plot. (a,b) $\tau_p = 1.0 \text{ ms}$, and $\text{APD} = 159 \text{ ms}$; (c,d) $\tau_p = 9.0 \text{ ms}$, and $\text{APD} = 194.4 \text{ ms}$; (e,f) $\tau_p = 11.0 \text{ ms}$, and $\text{APD} = 215.8 \text{ ms}$. The action potential is monitored at positions $x \simeq 0.26 \text{ cm}$ (right panels), and at $x \simeq 0.75 \text{ cm}$ (left panels).

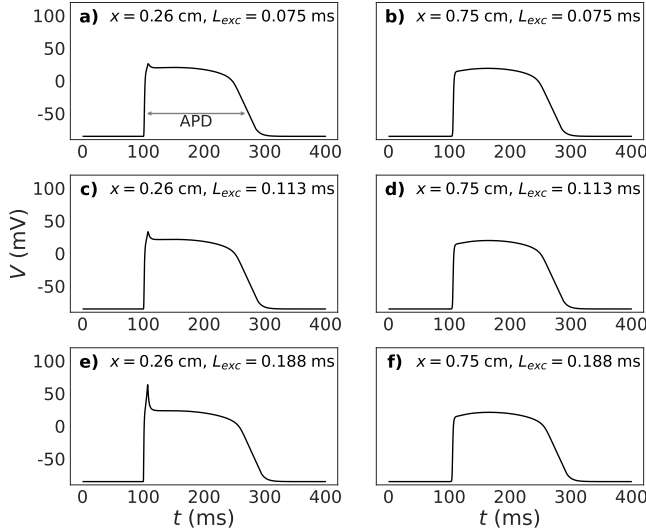


FIG. 4: The action potential V (black curves) in natural units as a function of time t excited by a single rectangular pulse current with amplitude $J_{\text{amp}} = 4 \text{ mA}$, and duration $\tau_p = 7 \text{ ms}$ (not shown). The action potential duration (APD), indicated by the gray horizontal double-headed arrow, is measured for each plot. (a,b) $L_{\text{exc}} = 0.075 \text{ cm}$, and $\text{APD} = 173.9 \text{ ms}$; (c,d) $L_{\text{exc}} = 0.113 \text{ cm}$, and $\text{APD} = 174.9 \text{ ms}$; (e,f) $L_{\text{exc}} = 0.188 \text{ cm}$, and $\text{APD} = 179.5 \text{ ms}$. The action potential V is monitored at $x \simeq 0.25 \text{ cm}$ (right panels), and at $x \simeq 0.75 \text{ cm}$ (left panels).

III. RESULTS

A. The Action Potential

Using Eq. (21-23), we have calculated numerically the ventricular AP propagating through ventricular tissue of length $L = 3 \text{ cm}$ as a function of time t . A small segment of the tissue/cable of length $L_{\text{exc}} = 0.11 \text{ cm}$ is initially excited through its left end, i.e., the segment from $x = 0$ to $x = L_{\text{exc}} = 0.11 \text{ cm}$, using stimulus currents of amplitude $J_{\text{amp}} = 5 \text{ mA}$ and different durations τ_p . Typical AP pulse profiles (black curves) along with the associated stimulus currents (red curves) are shown in Fig. 3, monitored at two different locations on the cable, i.e., at $x \simeq 0.26 \text{ cm}$ (relatively close to the excited region, left panels) and $x \simeq 0.75 \text{ cm}$ (at one-fourth of the cable length as measured from $x = 0$, right panels). As it can be observed, the amplitude of the AP as well as its duration (action potential duration, APD) increases with increasing τ_p (from top to bottom). The latter, specifically, which is defined as the width of the pulse at 12% of its maximum amplitude (illustrated in (a) by the gray horizontal double-headed arrow), increases from 159 ms for $\tau_p = 1.0 \text{ ms}$, to 194.4 ms for $\tau_p = 9.0 \text{ ms}$, to 215.8 ms for $\tau_p = 9.0 \text{ ms}$. Left and right panels, obtained by monitoring the AP pulses at different locations on the cable, also differ in that the former exhibit a sharp peak at a time instant corresponding to the end of the stimulus current pulse. This sharp peak decreases until it practically vanishes for locations on the cable relatively far from the excited region.

Similarly, in Fig. 4, the calculated action potential V as a function of time t is monitored at two different positions on the cable for stimulus currents of amplitude $J_{\text{amp}} = 4 \text{ mA}$, duration $\tau_p = 4 \text{ ms}$, and three different values of the initially excited segment at the left end of the cable of length L_{exc} , which extends from $x = 0$ to $x = L_{\text{exc}}$. As in Fig. 3, the action potential is monitored at $x \simeq 0.25 \text{ cm}$ and $x \simeq 0.75 \text{ cm}$ (left and right panels, respectively). Again it is observed that, the duration of the action potential (APD) increases with increasing L_{exc} . Specifically, the APD increases from 173.9 ms for $L_{\text{exc}} = 0.075 \text{ cm}$ to 174.9 ms for $L_{\text{exc}} = 0.113 \text{ cm}$, to 179.5 for $L_{\text{exc}} = 0.113 \text{ cm}$. In both Figs. 3 and 4, the action potential exhibits the right characteristics in (e) and (f) panels, as long as the shape and the width (i.e., the APD) is concerned.

B. The pseudo-ECG

The analysis and interpretation of ECGs remains mostly empirical. The pseudo-ECG at a particular time-instant t is calculated numerically from the spatial profile of the AP at that time-instant on the cable using the expression [8, 23, 24, 36, 37] (for a thorough derivation see Ref. [38])

$$\Phi_e(\mathbf{x}^*, t) = -K \int \nabla V(\mathbf{x}, t) \cdot \nabla \frac{1}{|\mathbf{x}^* - \mathbf{x}|} d\mathbf{x}, \quad (24)$$

where $\nabla V(\mathbf{x}, t)$ is the spatial gradient of the ventricular AP, $K = 1.89 \text{ mm}^2$ is a constant that depends on electrophysiology.

ical quantities, such as the radius of the fiber and the intracellular conductivity. The “electrode” measuring the voltage is at point \mathbf{x}^* of the fiber, and $|\mathbf{x}^* - \mathbf{x}|$ is the distance from a source point \mathbf{x} to a field point \mathbf{x}^* ($\mathbf{x}^* > \mathbf{x}$). The temporal profile of the pseudo-ECG Φ_e constitutes an approximation for the ventricular component of the ECG, i.e., the pseudo-ECG generated at a hypothetical electrode which is located at a particular distance away from the last epicardial cell along the cable. As shown in Fig. (1), the ventricular potential contributes specifically to the formation of the QRS cluster and the T wave. The pseudo-ECG is, thus, expected to reproduce these features.

In one dimension, Eq. (24) reads

$$\Phi_e(x^*, t) = -K \int \frac{\partial V(x, t)}{\partial x} \left(\frac{\partial}{\partial x} \frac{1}{|x^* - x|} \right) dx. \quad (25)$$

We calculate the pseudo-ECG for point outside the cell cable, so for $x^* > L$, Eq. (25) becomes

$$\Phi_e(x^*, t) = -K \int \frac{\partial V(x, t)}{\partial x} \frac{1}{(x^* - x)^2} dx, \quad (26)$$

and is thus more easily calculated. Using the spatial profiles calculated from Eq. (21) - (23) at each time instant, we calculate $\Phi_e(L, t)$ which is the desired pseudo-ECG; in our calculations $x^* = 3.37$ cm, while the cell cable length is $L = 3.0$ cm. As shown in Fig. 5, the T-wave has positive polarity and its amplitude is defined as the vertical distance from $V = 0$. In general, T waves are considered positive when their deflection is upward, and negative when it is downward. For *biphasic T-waves* (waves with both an upward and a downward deflection), unless otherwise stated, the dominant deflection is chosen. In the small inset, a surface ECG which is recorded using two electrodes placed on the skin surface, away from the heart, is visually compared to the pseudo-ECG.

C. Constant Diffusion Coefficient

We first run our model with a spatially constant diffusion coefficient $\tilde{D} = D_0$. This can be regarded as an effective parameter, a mean value to account for the discontinuity defect part inserts. The height of the R-wave (see blue star in Fig. 5) in each pseudo-ECG denotes the value of the T-wave amplitude in units of mV; when plotted for 25 different values, as shown in Fig. 6, it appears to exhibit an exponential dependence on the effective diffusion coefficient \tilde{D} . Since repeated attempts to fit a single exponential curve using least squares failed, we tried using the sum of two exponentials via the *ansatz*

$$R_{wa} = A e^{-\alpha \tilde{D}} + B e^{-\beta \tilde{D}} + C, \quad (27)$$

where R_{wa} is the R-wave amplitude, and A , α , B , β , and C , are parameters to be fitted. Using the *ansatz* (27), we obtained excellent fit using parameters $A = 0.79$, $\alpha = 115.36$, $B = 0.56$, $\beta = 1258.84$, and $C = 0.595$. In the exemplary fit shown by the blue line in Fig. 6, we notice a transition region around the value of 0.0012 ± 0.0002 $\text{cm}^2\text{ms}^{-1}$ of the diffusion coefficient, which, as mentioned before, is an experimental value used frequently in literature. The transition region

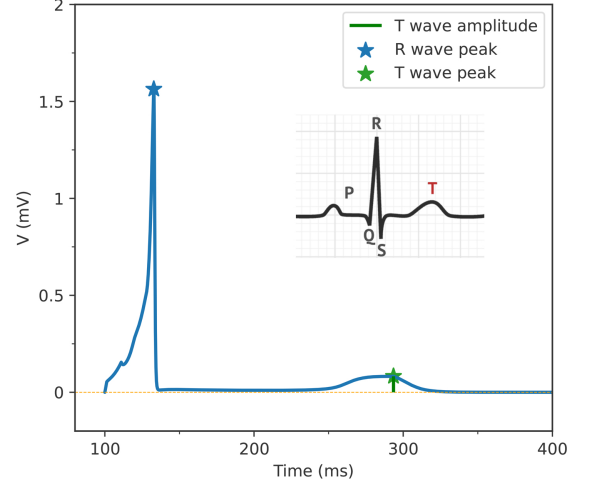


FIG. 5: Simulated pseudo-ECG as a function of time t calculated using the three-variable Fenton-Karma model. For comparison, a drawing of a real ECG is shown in the inset. We can clearly detect the R and T wave equivalents whose amplitudes we designate with the blue and green stars respectively.

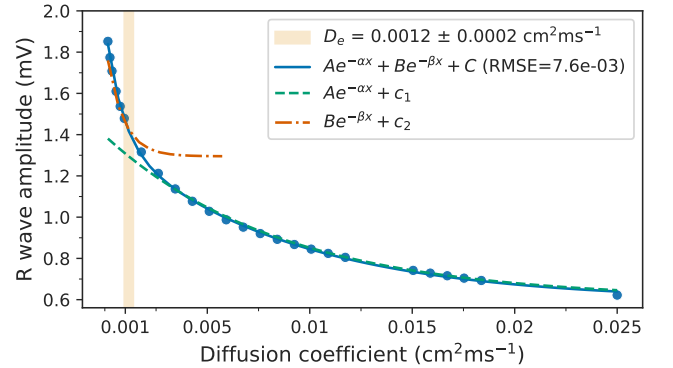


FIG. 6: R-wave amplitude as a function of the (homogeneous, spatially constant) voltage diffusion coefficient $\tilde{D} = D_0$, extracted from the calculated pseudo-ECGs using Eq. (25) for a total of 25 values for D_0 within the interval $0.0005 - 0.025$ $\text{cm}^2\text{ms}^{-1}$. Other simulation parameters are: $J_{amp} = 10.0$ mA, $t_p = 10.0$ ms, $L_{exc} = 0.105$ cm, $dx = 0.0075$ cm, $dt = 0.0013$ ms, $N_{steps} = 230769$. Curve fit parameters are: $A = 0.79$, $\alpha = 115.36$, $B = 0.56$, $\beta = 1258.84$, and $C = 0.595$. The range of values $D_e = (0.0012 \pm 0.0002)$ $\text{cm}^2\text{ms}^{-1}$ denoted by the shaded area, is a range of experimental values used frequently in the literature. The constants for the failed single exponentials are $c_1 = 0.6$ (green curve), and $c_2 = 1.3$ (red curve).

is identified by those values of $\tilde{D} = D_0$ for which the fitted single-exponential curves $A e^{-\alpha \tilde{D}} + C_1$ (green-dashed curve) and $B e^{-\beta \tilde{D}} + C_2$ (red dashed-dotted curve) start diverging significantly from the numerical data (slightly above the experimental value of $\tilde{D} = D_e$). The algorithm was implemented using the SciPy python library.

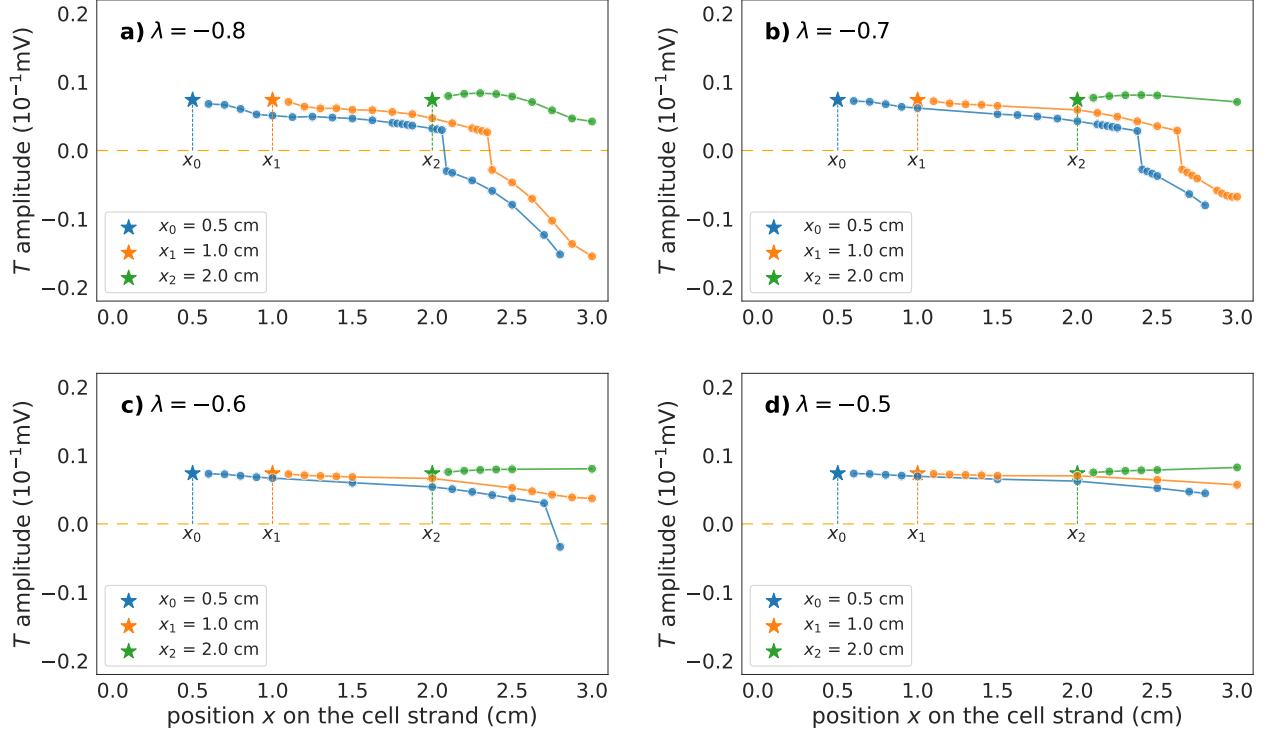


FIG. 7: T-wave morphology depicted as magnitude of the peak or the dip of the T-wave (in units of mV) for various starting positions and widths of the defected tissue. The variable x ($0 < x < L$) is the position on the cell strand. The star at each x_j ($j = 0, 1, 2$) marks the position of the beginning of the defect for three different values of $x_{\text{scar}} = 0.5, 1.0$, and 2.0 . All results are color-coded by this value. The location of each dot on the x -axis signifies the end point of the defected region at $x_{\text{scar}} + L_{\text{scar}}$, i.e., the distance along the x -axis of the dot from the star on the same curve represents the value of L_{scar} . Each plot has a different value for the parameter λ as indicated in the label on top. For all four subplots, the effective diffusion coefficient is $D_0 = 0.005 \text{ cm}^2 \text{ ms}^{-1}$.

D. Modeling a Space-Dependent Diffusion Coefficient

To study the polarization of the T-wave in a tissue containing a localized defect, a stimulus current in the form of a rectangular pulse of amplitude $J_{\text{amp}} = 0.9 \text{ mA}$, and duration $\tau_p = 11 \text{ ms}$, was applied at the first 15 cells of the cable, those which are at its left end ($x = 0$), whose length is $L_{\text{exc}} \simeq 0.011 \text{ cm}$. Then, the pseudo-ECG is calculated from the spatio-temporal profile of the APs, and the maximum magnitude of the T-wave is identified. This procedure was repeated as a function of the width of the defect L_{scar} for three different values of the position of the onset of the defect x_{scar} and four values of the parameter λ . The results are presented in a compact way in Fig. 7. In all four subfigures, the diffusion coefficient in the healthy region is $D_0 = 0.005 \text{ cm}^2 \text{ ms}^{-1}$. The defect was modeled using a spatially dependent diffusion coefficient $\tilde{D}(x)$, whose characteristics were previously depicted in Fig. 2. For the results presented in Fig. 7, the defected region spans the interval from $x = x_{\text{scar}}$ to $x = x_{\text{scar}} + L_{\text{scar}}$. Within this interval, the diffusion coefficient is $\tilde{D} = L_{\text{scar}}$, with $\lambda = -0.8, -0.7, -0.6$, and -0.5 in Fig. 7(a), (b), (c), and (d), respectively. Obviously, the relation $x_{\text{scar}} + L_{\text{scar}} < L$ should hold in any case.

By inspection of Fig. 7 we observe that the curves for $x_{\text{scar}} = x_3 = 2 \text{ cm}$ (green curves) always remain on the pos-

itive side of the vertical axis, meaning that in this case there is no polarization inversion of the corresponding T-wave, and thus this is always positive. The same holds true for any other value of $x_{\text{scar}} > 2$, since the defected region constitutes only a relatively small part of the cable, which is of length $L = 3 \text{ cm}$, so that it cannot affect significantly the spatio-temporal AP profile. It can be also observed from Fig. 7(d) that all three curves remain on the positive sides of the vertical axis, and thus no T-wave inversion appears, due to the relatively small magnitude of λ . Indeed, the magnitude of λ in this case does not seem to be sufficiently high (or equivalently the defect is not sufficiently deep) to invert T waves. For slightly deeper defect, for $\lambda = -0.6$, as shown in Fig. 7(c), T-wave inversion is observed for $x_{\text{scar}} = x_0 = 0.5$ and $L_{\text{scar}} = 2.25$ (blue curve) but not for $x_{\text{scar}} = x_1 = 1.0$ or $x_{\text{scar}} = x_2 = 2.0$ (orange and green curves, respectively). The obvious reason is that in the latter cases the width of the defected region L_{scar} cannot reach such a high value as that in the former case ($L_{\text{scar}} = 2.25$). Moreover, as it can be observed from Figs. 7(a) and (b) the parts of the curves with $x_{\text{scar}} = x_0 = 0.5$ (blue curves) and $x_{\text{scar}} = x_1 = 1.0$ (orange curves), respectively, with inverted (negative) T-wave become larger with decreasing λ . From these observations can thus be concluded that for fixed x_{scar} , deep and wide defected regions favor T-wave inversion. Furthermore, the value of L_{scar} at the tran-

sition from positive to negative T waves is lower in the orange curves ($x_{\text{scar}} = x_1 = 1.0$) than that in the blue curves ($x_{\text{scar}} = x_0 = 0.5$) as can be observed from Figs. 7(a) and (b). Thus, for fixed λ , defects with higher x_{scar} are capable to invert T-waves with lower L_{scar} . From the above remarks it becomes clear that the width, the depth, and the starting position of the defect contribute decisively to T-wave morphology.

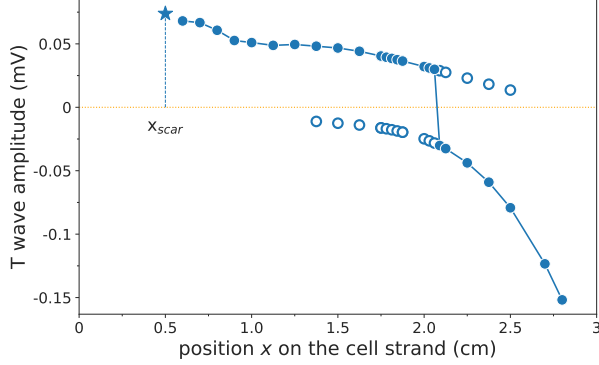


FIG. 8: T-wave maximae and minimae as a function of the width of the defected region L_{scar} , as obtained from the pseudo-ECG with inhomogeneous voltage diffusion coefficient $\tilde{D}(x)$ with $D_0 = 0.005 \text{ cm}^2 \text{ ms}^{-1}$ and $\lambda = -0.8$. The defected regions start at $x_{\text{scar}} = 0.5 \text{ cm}$. The blue solid curve is a guide to the eye. The representation is the same as that in Fig. 7. The points depicted as blue solid circles are the ones chosen as the largest of the two in the biphasic wave. The hollow white circles show the amplitude of the other wave in the biphasic phase. The truly biphasic phase is limited to a few points around the blue vertical segment at $L_{\text{scar}} \simeq 1.6$. The purpose of this plot is to show that there is a transition phase during T inversion, where the wave has both positive (upward) and negative (downward) parts.

We should note that the transition from positive to negative T waves is realized through a biphasic stage, with a minimum and a maximum of similar magnitude. This is consistent with the bibliography where it is reported that biphasic T waves usually evolve and are often followed by T-wave inversion with strongly suspected myocardial ischaemia [39]. There was no attempt made to trace the biphasic stage in Fig. 7, which is actually limited within a small interval around the transition point. Wherever two extremae appear in the calculated T-wave, only the higher of them is plotted. However, a typical biphasic stage of the calculated T-wave is illustrated below.

In Fig. 8, the maximum and the minimum of the T-wave (equivalently the maximum and the second maximum of the magnitude of the T-wave) are plotted as a function of the width of the defected region L_{scar} , for the parameters of the blue curve in Fig. 7(a). Recall that all points on that curve were obtained from the pseudo-ECG using voltage diffusion coefficient \tilde{D} with $D_0 = 0.005 \text{ cm}^2 \text{ ms}^{-1}$, $\lambda = -0.8$, and a defected region starting at $x_{\text{scar}} = x_0 = 0.5 \text{ cm}$. The blue circles (filled and empty) have been obtained through numerical calculations while the (blue) solid curve is a guide to the eye, actually indicating the transition from positive to negative (inverted) T-wave. The filled and empty circles indicate maximae and

second maximae (whenever they exist) of the T-wave magnitude. Note that the truly biphasic stage, for which the minimum and the maximum of the T-wave have approximately equal magnitude, is limited to a few (~ 5) points around the blue vertical segment indicating the T-wave inversion transition. Further away from that segment, e.g., at $x = 1.5 \text{ cm}$, i.e., at $L_{\text{scar}} = 1.0$, the maximum of the T-wave has much larger magnitude of the minimum, and thus the positive character of the T-wave is dominant. Such cases are regarded as positive T-waves in Fig. 7. Correspondingly, cases in which the negative (inverted) character of the T-wave is dominant are regarded as inverted T-waves in Fig. 7.

In Fig. 9, the pseudo-ECG as a function of time t , the map of the action potential on the $x-t$ plane, and the three-dimensional plot of the action potential on the $x-t$ plane are shown in three different widths L_{scar} of the defected region of the cardiac tissue, to illustrate its effect on the spatio-temporal profile of the action potential and eventually on the T-wave morphology. In the figure, from the first to third row (from top to bottom), the T-wave of the pseudo-ECG is positive, biphasic, and negative (inverted), respectively. The results shown on the first row have been obtained for a healthy tissue, that is, for an averaged diffusion coefficient \tilde{D} which is homogeneous (without defected region, $\lambda = 0$). In this case, as shown in the map on the second column, the width of the action potential decreases monotonically as it propagates from the excitation region of the cable outwards. This is also apparent from the three-dimensional plot, where it is also clear that the amplitude of the pulse is not significantly affected during propagation. The sharp peak of the action potential profile, appearing in all three sub-figures in Fig. 9, is due to the action potential pulse being very close to or inside the excitation region of length $L_{\text{exc}} = 0.11 \text{ cm}$ of the cable. That peak however disappears after short time of propagation in all three cases.

The results shown in the second and third row have been obtained with a diffusion coefficient $\tilde{D} = \tilde{D}(x)$, as in Eq. (13), with $L_{\text{scar}} = 1.25 \text{ cm}$ and $L_{\text{scar}} = 1.5 \text{ cm}$, respectively. AS it can be observed, the results in the second and third row are significantly affected by the existence of the defected region. In the second row the T-wave of the pseudo-ECG becomes biphasic, while the width of the action potential pulse is not any more monotonically decreasing during outward propagation. Instead, the pulse narrows substantially and abruptly while it propagates into the defected region, and becomes wider after departing from it. That effect is also visible in the three-dimensional plot, where we may also observe that the amplitude of the AP is not significantly affected during propagation, even in the defected region. In the third row, the T-wave of the pseudo-ECG is inverted, becoming negative. The profile of the propagating AP pulse is in this case very similar to that shown in the second row, i.e., it narrows substantially and abruptly when entering the defected region and widens again when departing from it. In this case however the pulse narrows within a larger interval because of the larger $L_{\text{scar}} = 1.5 \text{ cm}$. The three-dimensional plot is also very similar to that in the second row.

These figures clearly illustrate the effect of the defected region on the propagation of the action potential which in turn

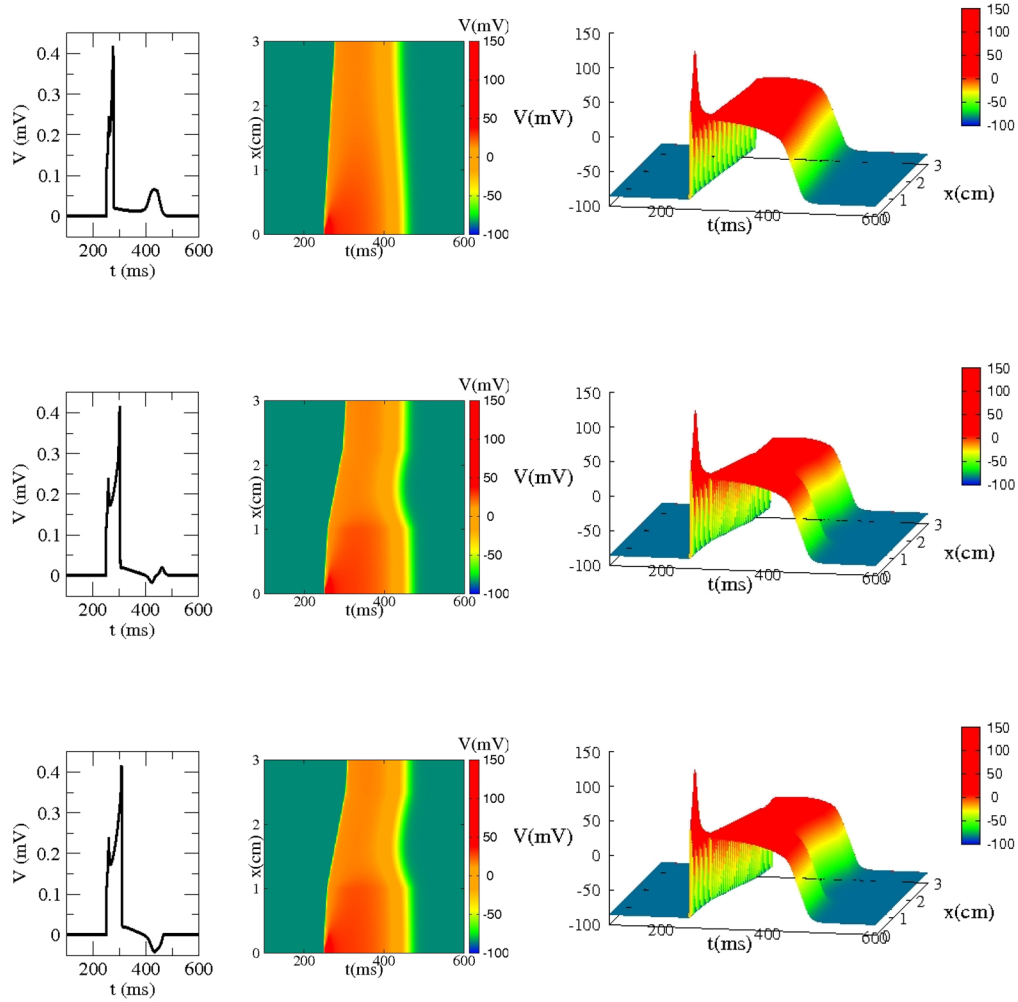


FIG. 9: Pseudo-ECGs as a function of time t , two-dimensional maps of the action potential on the $x-t$ plane, and three dimensional plots of the action potential on the $x-t$ plane, are shown on the left, middle, and right columns, respectively. The parameters, from top to bottom row are $L_{\text{scar}} = 0$ (first row), $L_{\text{scar}} = 1.25$ cm (second row), and $L_{\text{scar}} = 1.5$ cm (third row). The first, second, and third row show the case of pseudo-ECG with positive, biphasic, and negative (inverted) T-wave, respectively. These figures illustrate the effect of the defected region on the spatio-temporal profile of the action potential. The defected region in the second and third row starts at $L_{\text{scar}} = 0.5$, and the length of the cable is $L = 3$ cm in all three rows.

affect the pseudo-ECG and is capable of inverting the T-wave. In Fig. 9, no attempt was made to match observed ECG data. This would require to choose the constant K in Eq. (26) and other parameters appropriately. But this is outside the scope of this work which aims at showing qualitatively that spatially inhomogeneous voltage diffusion coefficients can account for the inversion of the T-wave, and also to account for the variation of the R-wave amplitude against a homogeneous (constant) diffusion coefficient $\bar{D} = D_0$.

IV. CONCLUSIONS

We used the “simple” FK3V model to simulate the dynamics of the action potential propagation in a cable and calculate a pseudo-ECG that reproduces the R wave and the T wave of

an observed ECG. To the best of our knowledge, pseudo-ECG calculation using the FK3V model has not been reported before. Our results connect the propagation of electrical (action) potentials within the cardiac tissue with the morphology of the pseudo-ECG, and by extension with what physicians actually observe i.e., the ECG. Specifically, our results reveal the dependence of the R-wave amplitude as a function of the (homogeneous) voltage diffusion coefficients and, most importantly they point towards an intimate relation between inhomogeneous diffusion coefficients (diffusion coefficients with defected regions) and the inversion (of the polarity) of the T-wave. The latter is often observed in cases of ischemia in ECG recordings by physicians.

Defected regions in the diffusion coefficient represent “scars” in the cardiac tissue where the electrical connection between cells is broken due to destruction of the gap junctions,

as e.g., occurs in ischemia. As a result, the electrical conductance is reduced considerably in these defected region(s), leading unavoidably to a severe reduction of the diffusion coefficient there. For sufficiently large and deep defected regions in the diffusion coefficient, the ability of the cardiac tissue to conduct the action potential is strongly affected, and as a result the calculated pseudo-ECG exhibits T-wave inversion. Such findings in observed ECGs are often related to ischemia.

It should be mentioned, however, that T-wave inversion could be also obtained using a spatially constant, averaged diffusion coefficient $\langle \tilde{D} \rangle = D_0$ for sufficiently small values of D_0 . This could represent the case of many small scars distributed almost uniformly along the cardiac tissue (the cable), and it is a matter of future work. Our approach to use a single-cell wide strand of cardiac cells for action potential propagation in a one-dimensional cable was dictated by reasons of simplicity.

While 1D numerical simulations capture essential aspects of the cardiac electrical action such as its R and T wave morphology, our approach can be certainly extended straightforwardly in more dimensions in the future. The results obtained here for the T-wave inversion and its dependence on the diffu-

sion coefficient configuration (the inhomogeneity) may ignite research on solving the inverse problem, i.e., on how to locate a defected/ischemic region in the cardiac tissue from observed ECG data.

Acknowledgments

Computations in this paper were run in part on the FASRC cluster supported by the FAS Division of Science Research Computing Group at Harvard University. GPT and GDB acknowledge support by the research project co-funded by the Stavros Niarchos Foundation (SNF) and the Hellenic Foundation for Research and Innovation (H.F.R.I.) under the 5th Call of “Science and Society” Action – “Always Strive for Excellence – Theodore Papazoglou” (Project Number: 011496). Authors NL and IK gratefully acknowledge financial support from Khalifa University of Science and Technology, Abu Dhabi, United Arab Emirates, via the project CIRA-2021-064 (8474000412).

-
- [1] P. W. Macfarlane, A. van Oosterom, O. Pahlm, P. Kligfield, M. Janse, and J. E. Camm, *Comprehensive Electrocardiology* (Springer London, London, 2010), 2nd ed., ISBN 1848820453, URL <https://doi.org/10.1007/978-1-84882-046-3>.
 - [2] A. G. Kléber and Q. Jin, *Biophys Rev.* **2**, 031301 (2021), URL <https://doi.org/10.1063/5.0050192>.
 - [3] S. Alonso, M. Bär, and B. Echebarria, *Rep. Prog. Phys.* **79**, 096601 (56pp) (2016), URL <https://dx.doi.org/10.1088/0034-4885/79/9/096601>.
 - [4] P. C. Franzone, L. F. Pavarino, and S. Scacchi, Springer International Publishing Switzerland (2014), URL <https://doi.org/10.1007/978-3-319-04801-7>.
 - [5] Y. C. Ji and F. H. Fenton, *Am. J. Phys.* **84**, 626 (2016), URL <https://doi.org/10.1119/1.4953167>.
 - [6] S. Golemati and K. S. E. Nikita, Springer Nature Singapore Pte Ltd. 2019 (2019), URL <https://doi.org/10.1007/978-981-10-5092-3>.
 - [7] F. Fenton and A. Karma, *Chaos* **8**, 20 (1998), URL <https://doi.org/10.1063/1.166311>.
 - [8] A. Bueno-Orovio, E. M. Cherry, and F. H. Fenton, *Journal of Theoretical Biology* **253**, 544 (2008), URL <https://doi.org/10.1016/j.jtbi.2008.03.029>.
 - [9] C. D. Marcotte, M. J. Hoffman, F. H. Fenton, and E. M. Cherry, *Chaos* **33**, 093141 (2023), URL <https://doi.org/10.1063/5.0156314>.
 - [10] Z. Zhang and O. Steinbock, *Chaos* **27**, 093921 (2017), URL <https://doi.org/10.1063/1.5000225>.
 - [11] C. D. Marcotte, F. H. Fenton, M. J. Hoffman, and E. M. Cherry, *Chaos* **31**, 013118 (2021), URL <https://doi.org/10.1063/5.0033539>.
 - [12] G. W. Beeler and H. Reuter, *J. Physiol.* **268**, 177 (1977), URL <https://doi.org/10.1113/jphysiol.1977.sp011853>.
 - [13] C.-H. Luo and Y. Rudy, *Circulation Research* **68**, 1501 (1991), URL <https://doi.org/10.1161/01.RES.68.6.1501>.
 - [14] K. H. W. J. Ten Tusscher, D. Noble, P. J. Noble, and A. V. Panfilov, *Am. J. Physiol. Heart Circ. Physiol.* **286**, H1573 (2004), URL <https://doi.org/10.1152/ajpheart.00794.2003>.
 - [15] K. C. Siontis, P. A. Noseworthy, Z. I. Attia, and P. A. Friedman, *Nat Rev Cardiol* **18**, 465 (2021), ISSN 1759-5002.
 - [16] E. Angelaki, M. E. Marketou, G. D. Barmparis, A. Patrianakos, P. E. Vardas, F. Parthenakis, and G. P. Tsironis, *The Journal of Clinical Hypertension* (Greenwich, Conn.) **23**, 935 (2021).
 - [17] R. Hagan, C. J. Gillan, and F. Mallett, *Informatics in medicine unlocked* **24**, 100606 (2021), ISSN 2352-9148.
 - [18] B. Tutuko, A. Darmawahyuni, S. Nurmaini, A. E. Tondas, M. Naufal Rachmatullah, S. B. P. Teguh, F. Firdaus, A. I. Sapitri, and R. Passarella, *PloS one* **17**, e0277932 (2022), ISSN 1932-6203.
 - [19] A. L. Wit, *The ventricular arrhythmias of ischemia and infarction : electrophysiological mechanisms* (Futura Pub. Co., Mount Kisco, NY, 1993), ISBN 0879933763.
 - [20] D. P. Zipes, J. Jalife, and W. G. Stevenson, *Cardiac electrophysiology : from cell to bedside* (Elsevier, Philadelphia, PA, 2018), 7th ed.
 - [21] R. M. Shaw and Y. Rudy, *Cardiovascular Research* **35**, 256 (1997), ISSN 0008-6363.
 - [22] H. J. Jongsma and R. Wilders, *Circulation Research* **86**, 1193 (2000), ISSN 0009-7330.
 - [23] O. V. Aslanidi, R. H. Clayton, J. L. Lambert, and A. V. Holden, *Journal of Theoretical Biology* **237**, 369 (2005), URL <https://doi.org/10.1016/j.jtbi.2005.04.022>.
 - [24] K. Q. Wang, Y. F. Yuan, Y. Y. Tang, and H. Zhang, in *Computers in Cardiology* (2006), pp. 673–676.
 - [25] A. L. Hodgkin and A. F. Huxley, *J. Physiol.* **117**, 500 (1952), URL <https://doi.org/10.1113/jphysiol.1952.sp004764>.
 - [26] F. Fenton and A. Karma, *Chaos* **8**, 879 (1998), URL <https://doi.org/10.1063/1.166374>.
 - [27] S. Rohr, *Cardiovascular Research* **62**, 309 (2004), ISSN 0008-6363, URL <https://doi.org/10.1016/j.cardiores.>

- 2003.11.035.
- [28] J. Bragard, A. Witt, D. Laroze, C. Hawks, J. Elorza, I. R. Cantalapiedra, A. Penaranda, and B. Echebarria, *Chaos* **31**, 073144 (2021), URL <https://doi.org/10.1063/5.0053651>.
 - [29] H. P. Langtangen and S. Linge, *Finite Difference Computing With Pdes : a Modern Software Approach*, vol. 16 of *Texts in Computational Science and Engineering* (Springer Open, Cham, 2017), ISBN 9783319554556.
 - [30] M. D. Lesh, M. Pring, and J. F. Spear, *Circulation Research* **65**, 1426 (1989), URL <https://doi.org/10.1161/01.RES.65.5.1426>.
 - [31] J. W. Cain, E. G. Tolkacheva, D. G. Schaeffer, and D. J. Gauthier, *Phys. Rev. E* **70**, 061906 (2004), URL <https://doi.org/10.1103/PhysRevE.70.061906>.
 - [32] R. A. Oliver and W. Krassowska, *Annals of Biomedical Engineering* **33**, 907 (2005), URL <https://doi.org/10.1007/s10439-005-3948-3>.
 - [33] A. Peñaranda, I. R. Cantalapiedra, J. Bragard, and B. Echebarria, *Theoretical Biology and Medical Modelling* **9**, 50 (2012), URL <https://doi.org/10.1186/1742-4682-9-50>.
 - [34] F. H. Fenton, E. M. Cherry, H. M. Hastings, and S. J. Evans, *Chaos* **12**, 852 (2002), URL <https://doi.org/10.1063/1.1504242>.
 - [35] E. G. Tolkacheva, D. G. Schaeffer, D. J. Gauthier, and C. C. Mitchell, *Chaos* **12**, 1034 (2002), URL <https://doi.org/10.1063/1.1515170>.
 - [36] K. Gima and Y. Rudy, *Circ. Res.* **90**, 889 (2002), URL <https://doi.org/10.1161/01.RES.0000016960.61087.86>.
 - [37] R. H. Clayton and A. V. Holden, *Progress in Biophysics and Molecular Biology* **85**, 473 (2004), URL <https://doi.org/10.1016/j.pbiomolbio.2003.12.002>.
 - [38] R. Plonsey and R. C. Barr, *Bioelectricity: A Quantitative Approach* (Springer Nature, Netherlands, 2007), 3rd ed., ISBN 0387488650.
 - [39] K. Channer and F. Morris, *BMJ* **324**, 1023 (2002), ISSN 0959-8138.